




Hybrid stimulated Raman scattering–two-plasmon decay instability and 3/2 harmonic in steep-gradient femtosecond plasmas

I. Tsymbalov ^{1,2,*}, D. Gorlova ^{1,2} and A. Savel'ev ^{1,3}

¹*Faculty of Physics and International Laser Center, Lomonosov Moscow State University, 119991, Moscow, Russia*

²*Institute for Nuclear Research of Russian Academy of Sciences, 117312, Moscow, Russia*

³*Lebedev Physical Institute of Russian Academy of Sciences, 119991, Moscow, Russia*



(Received 29 June 2020; accepted 18 November 2020; published 14 December 2020)

We numerically study interaction of a very intense ($I \sim 10^{17}$ to 5×10^{19} W/cm²) femtosecond obliquely incident p -polarized laser pulse with a steep-gradient ($L \sim \lambda$) plasma, i.e., within the conditions typical for modern experiments. It is shown that the hybrid stimulated Raman scattering–two-plasmon decay instability develops near the quarter-critical density surface and plays the dominant role for the plasma waves' excitation and energy absorption. The plasmons are excited as two wave packets confined near this surface with very wide $\approx \omega_0/c$ spatial spectra along its normal. Hence, phase-matching conditions for the 3/2 harmonic generation are fulfilled immediately and include the mechanism coming from the high harmonics of plasma waves. This mechanism has been proved experimentally by observing an additional 3/2 harmonic beam.

DOI: [10.1103/PhysRevE.102.063206](https://doi.org/10.1103/PhysRevE.102.063206)

I. INTRODUCTION

Parametric instabilities in a dense laser plasma have been actively studied for decades due to extensive research on ICF and related phenomena [1–3]. Here inhomogeneity of plasma density n_e is weak [i.e., laser wavelength λ is much less than the plasma scale length $L = (\frac{\partial \ln n_e}{\partial y})^{-1}$] due to the moderate intensities of nanosecond laser radiation $I \sim 10^{14}$ to 10^{16} W/cm² [4,5]. Parametric plasma wave excitation differs greatly if shorter and relativistically intense laser pulses (intensity $I > 10^{18}$ W/cm²) are used: (1) increment of these instabilities is proportional to the laser field's amplitude, (2) amplitude of an excited plasma wave increases exponentially with time in the linear regime [5], and (3) preplasma, formed by an inevitable prepulse (nanosecond amplified spontaneous emission, short prepulses of various nature) or by the arbitrary long rising edge of the main pulse, is rather steep ($L \approx \lambda$) within the electron density range $n_e \sim 0.1\text{--}0.25n_c$ (n_c being critical density) [6], which confines the parametric excitation spatially.

Stimulated Raman scattering (SRS) in the homogeneous plasma has been intensively considered for the amplification of extremely intense ultrashort laser pulses [7,8] and electron acceleration [9]. Excitation of SRS and two-plasmon decay (TPD) instabilities by subrelativistic or relativistic femtosecond laser pulses in a long inhomogeneous plasma ($L \approx 10\text{--}100\lambda$) was studied in Refs. [10–15]. Parametric instabilities are also responsible for the formation of relativistic high-energy electron beams upon reflection of a powerful femtosecond laser pulse from a dense steep plasma [16,17].

Optical emission of the 3/2 harmonic (THH) is a characteristic feature of plasma instability onset at a quarter-critical density [14,15,18]. An angularly resolved emission spectrum

of this harmonic can be easily measured and carries information on the spatial spectra of plasma waves and their nonlinearity [19]. The possible impact of the hybrid SRS-TPD instability on the THH generation in a steep-gradient plasma (SGP; $L \sim \lambda$) was pointed out earlier from experimental data [18]. However, an overly simplified approximation of three plane waves was considered there, whereas strongly nonlinear plasma waves with a wide spatial spectra are excited in the SGP at relativistic intensities, being confined strongly in the direction normal to the plasma surface [20]. Also, in this simple plane wave approximation the excited plasmons do not satisfy the phase-matching conditions for generation of the THH immediately, and wave vectors of plasmons have to change due to their propagation along the plasma gradient before the THH is emitted. Earlier, in our mostly experimental paper [21], we discussed the acceleration of electrons for similar interaction parameters but only the simplified picture of electron acceleration was given with no plasma instability analysis.

In this work, we consider the excitation of plasma waves by relativistic femtosecond laser pulses in the SGP with 2D PIC simulations. The mechanism of plasma wave excitation and energy absorption—the hybrid SRS-TPD instability—is proved from the ponderomotive force analysis. We show that the phase matching conditions for the generation of THH are immediately fulfilled because of the wide spatial spectra of plasma waves in the SGP. We also discover and prove experimentally the mechanism of THH generation that considers the second harmonic of a nonlinear plasma wave.

II. NUMERICAL METHODS

Numerical simulations were performed using the fully relativistic 3D3V PIC code “Mandor” [22], reduced to the 2D3V variant. The simulation box size was $31 \times 14 \mu\text{m}^2$, spatial and temporal steps were $\lambda/100$ and 3×10^{-3} fs, respectively, and the total number of particles was 10^8 . The planar foil target consisted of cold electrons (initial temperature of 100 eV)

*ivankrupenin2@gmail.com

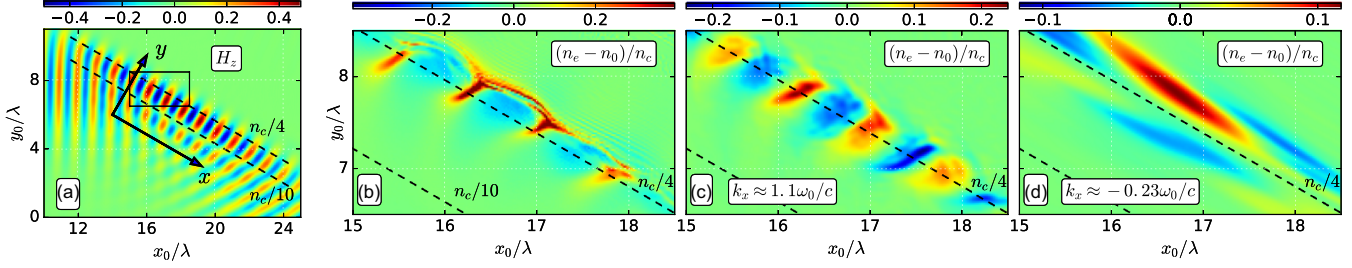


FIG. 1. Normalized laser pulse magnetic field H_z (a), electron density perturbations $(n_e - n_0)/n_c$ before (b) and after band-pass filtering in the vicinity of $k_x \approx 1.1 \frac{\omega_0}{c}$ (c) and $k_x \approx -0.23 \frac{\omega_0}{c}$ (d) within the rectangular windows shown in Fig. 2(b). Panels (b)–(d) show plasma density inside the black rectangle in panel (a). The x_0, y_0 axes correspond to the simulation domain, the x, y axes to the coordinate system in which spatial spectra in Figs. 2 and 3 are calculated after interpolation.

and immobile ions. A p -polarized laser pulse with Gaussian temporal and spatial envelopes, duration $\tau = 100$ fs (FWHM), diameter 4λ (FWHM), and central wavelength $\lambda = 1 \mu\text{m}$ entered the simulation box with its polarization in the xy plane (see Fig. 1). The preplasma profile was chosen as $n_0 \propto \exp(y/L)$ (y being the coordinate along normal to the target surface) with maximal density $10n_c$. Total simulation time was 360 fs with 1200 checkpoints written, which gave a frequency resolution $\sim 0.01\omega_0$ ($\omega_0 = 2\pi c/\lambda$ being the fundamental frequency). The maximum resolved frequency was $\sim 5\omega_0$.

III. TWO-PLASMON DECAY AND STIMULATED RAMAN SCATTERING

Only the TPD and SRS instabilities will remain in our study, as ions are assumed immobile at the femtosecond timescale. Let us first consider the interaction of a laser pulse with $I = 10^{17}$ W/cm² incident at an angle $\alpha = 60^\circ$ onto an $L = 1.25\lambda$ plasma gradient. This intensity is high enough to observe parametric instabilities but hinders strong plasma turbulence, which prevents clear unveiling of instabilities development. The turning surface of the laser radiation $n_{\text{turn}} = n_c/4$ for this angle corresponds to the maximum increment of parametric instabilities [5]. The magnetic field of the laser pulse H_z (normalized to $m c \omega_0 / e$, where m, e are an electron

mass and charge, respectively) is plotted in Fig. 1(a) and its spatial Fourier spectrum in Fig. 2(a). Initial data were zero padded outside the showed limits to obtain the required wave-number resolution of $0.01 \frac{\omega_0}{c}$. All our figures are shown at the instant when the intensity I at the turning point reaches its maximum, unless stated otherwise. The x -projection of the wave vector $k_{0x} = \frac{\omega_0}{c} \sin \alpha$ remains unchanged due to the choice of axis directions [23], while the y -projection changes from the $k_{0y} = \frac{\omega_0}{c} \cos \alpha$ for the incident radiation to the $-\frac{\omega_0}{c} \cos \alpha$ for the reflected one. These spatial harmonics form a wave packet localized near the turning surface in the case of the SGP.

Figures 1(b) and 2(b) present electron density perturbations and their spatial spectrum. It is clear that the spatial spectrum of plasma waves looks like the spatial spectrum of the laser pump. In the following, we denote plasma waves as κ and electromagnetic waves as k . As plasma wave spectra are wide in κ_y we will distinguish them by their κ_x projection. Two waves with $\kappa_{1x} \approx 1.1 \frac{\omega_0}{c}$ and $\kappa_{2x} \approx -0.23 \frac{\omega_0}{c}$ are amplified, while the pump wave has $k_{0x} \approx 0.87 \frac{\omega_0}{c}$. The wave numbers of the first plasmon κ_{1x} are close to $\frac{\omega_0}{c}$, which is typical for the SRS [5] and hybrid SRS-TPD [10] instabilities near the quarter-critical density. Next, we Fourier transformed the data in Fig. 2(b) back to the coordinate space using the two white

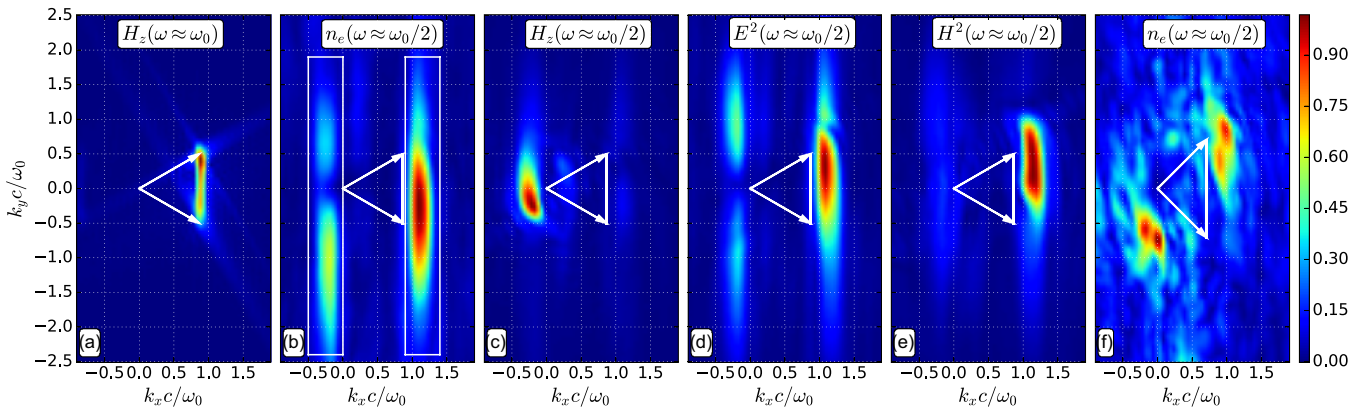


FIG. 2. Spatial spectra (normalized to their maxima) of the laser pulse field H_z [calculated from Fig. 1(a)] (a), plasma electron density [calculated from Fig. 1(b)] (b), H_z component of the Stokes wave (c), quantities E^2 (d), H^2 (e) [see explanation in the text; intensity $I = 10^{17}$ W/cm² and $\alpha = 60^\circ$ for panels (a)–(e)], and the electron density perturbations at $I = 10^{19}$ W/cm² and $\alpha = 45^\circ$ (f). Spatial spectra were obtained with preliminary Fourier bandpass filtering near the fundamental frequency ω_0 for panel (a) and near the plasma frequency $\omega_p \approx \omega_0/2$ for panels (b)–(f). Arrows correspond to the wave vectors of the incident and reflected laser pulses.

rectangular windows shown, thus filtering two plasmons [see Figs. 1(c) and 1(d)]. They are localized in a narrow ($\sim\lambda$) area in the vicinity of the quarter-critical density surface. The first plasmon [Fig. 1(c)] is directed along this surface, while the second one [Fig. 1(d)], consisting of almost a single spatial density oscillation, is directed nearly along the density gradient. Because of the low plasma temperature, these waves do not propagate outside the quarter-critical density area, where ponderomotive forces exciting them are localized.

IV. PONDEROMOTIVE FORCES ANALYSIS

Plasma waves of parametric instabilities are resonantly excited by the ponderomotive forces [24]. We have two longitudinal plasma waves $\mathbf{E}_1(\omega_1, \kappa_1)$ and $\mathbf{E}_2(\omega_2, \kappa_2)$, electromagnetic pump fields $\mathbf{E}_0(\omega_0, \mathbf{k}_0)$, $\mathbf{H}_0(\omega_0, \mathbf{k}_0)$, and scattered Stokes waves $\mathbf{E}_s(\omega_s, \mathbf{k}_s)$, $\mathbf{H}_s(\omega_s, \mathbf{k}_s)$. The latter waves arise when the pump wave is scattered by the plasma waves. The frequencies of the plasma waves are close to the plasma frequency $\omega_1 \approx \omega_2 \approx \omega_p$, $\omega_p \approx \omega_0/2$ near the quarter-critical density, and $\omega_s \approx \omega_0 - \omega_p \approx \omega_p$. To understand which components of the ponderomotive force amplify particular plasma waves we analyzed their spatial spectra. The simplest equation for the electron density n_e perturbation by the ponderomotive force $\boldsymbol{\pi}_0$ [24] in the homogeneous cold plasma can be written as $(\frac{\partial^2}{\partial t^2} + \omega_p^2)n_e \propto \nabla \cdot \boldsymbol{\pi}_0$. This expression is a linear one, hence a plasmon can be amplified by the ponderomotive force if their spatial components are collocated.

The force $\boldsymbol{\pi}_0 \propto -\nabla E^2$ describes both the TPD and SRS instabilities in a first approximation [24]. One can distinguish a part of this force $\propto -\nabla H^2$, which includes the beating of electromagnetic waves only. Comparing these two quantities, one can separate the contribution of both instabilities. We split the ponderomotive source into the resonant to the plasma wave (i.e., having frequencies near $\omega_0/2$) and nonresonant terms:

$$E^2 = \mathbf{E}_0(\omega_0) \cdot \mathbf{E}_1(\omega_0/2) + \mathbf{E}_0(\omega_0) \cdot \mathbf{E}_2(\omega_0/2) + \mathbf{E}_0(\omega_0) \cdot \mathbf{E}_s(\omega_0/2) + \text{nonresonant terms}, \quad (1)$$

$$H^2 = \mathbf{H}_0(\omega_0) \cdot \mathbf{H}_s(\omega_0/2) + \text{nonresonant terms}. \quad (2)$$

The resonant part of the ponderomotive force ∇E^2 can be calculated using a bandpass filter with central frequency $\omega_0/2$. Since the ∇ operator is linear, no spatial components will be missed if we consider E^2 without the ∇ operator.

The thus obtained spatial spectrum is shown in Fig. 2(d). It can be seen that the spectral components of the E^2 coincide with the spatial components of plasmons in Fig. 2(b), hence phase matching and amplification of both plasmons are possible. Equation (1) contains terms corresponding to the interference of the pump wave with both plasma and electromagnetic waves, while the resonant term in (2) contains only electromagnetic waves. The spatial component, which amplifies plasma waves with $\kappa_{1x} \approx 1.1 \frac{\omega_0}{c}$ only, predominates in the $H^2(\omega_0/2)$ spectrum [Fig. 2(e)]. This component comprises the backward Stokes electromagnetic wave having frequency $\omega_s \approx \omega_0/2$. Its spatial spectrum looks like the spectrum of the second plasmon with $\kappa_{2x} \approx -0.23 \frac{\omega_0}{c}$ [Fig. 2(c)].

Note that in an inhomogeneous plasma longitudinal waves may excite transverse electromagnetic waves and vice versa

[23]. This is why the spatial spectrum of the $H^2(\omega_0/2)$ source [Fig. 2(e)] has weak components at $k_x \approx -0.23 \frac{\omega_0}{c}$ as the $E^2(\omega_0/2)$ spectrum [Fig. 2(d)].

Amplification of the second plasma wave with $\kappa_{2x} \approx -0.23 \frac{\omega_0}{c}$ by the electromagnetic part of the ponderomotive force (through the SRS process) is forbidden since the corresponding $k_{sx} = k_{0x} - \kappa_{2x} \approx 1.1 \frac{\omega_0}{c}$ does not satisfy the dispersion relation $|k_s| < 0.5 \frac{\omega_0}{c}$. Thus the overall process can be described as the hybrid SRS-TPD instability: the \mathbf{E}_2 plasma wave is amplified by the beating of the plasma wave with the pump wave only, $\mathbf{E}_1 \cdot \mathbf{E}_0$, and corresponds to the TPD. The \mathbf{E}_1 is amplified by the beating of the electromagnetic Stokes and plasma waves with the pump wave, $\mathbf{E}_s \cdot \mathbf{E}_0 + \mathbf{E}_2 \cdot \mathbf{E}_0$, and is common for both the SRS and TPD processes. It should be noted that this hybrid SRS-TPD instability also can be regarded as some kind of high-frequency hybrid instability (HFHI) [1].

V. 3/2 HARMONIC GENERATION

The TPD instability may lead to the THH generation [15,18,25] with the current $\mathbf{j}_{\text{lin}} = \rho(\omega_0/2)\mathbf{v}_{\text{osc}}(\omega_0)$ being the source [here $\rho = -e(n_e - n_0)$, $\mathbf{v}_{\text{osc}}(\omega_0)$ is an electron quiver velocity in the laser field]. This radiation is widely used for laser plasma diagnostics [26].

The phase-matching conditions

$$\mathbf{k}_{1(2)} = \kappa_{1(2)} + \mathbf{k}_0, \quad \omega_{3/2} = \omega_p + \omega_0 \quad (3)$$

have to be fulfilled for the frequency $\omega_{3/2} \approx 3/2\omega_0$ and the wave vectors $\mathbf{k}_{1,2}$ of the harmonic. This cannot occur in a long scale length plasma ($L \gg \lambda$) immediately at the quarter-critical density surface [18]: wave vectors of plasmons should be tuned during their propagation in an inhomogeneous plasma. Hence, the excitation of plasma waves and THH generation are separated in space.

By contrast, the phase-matching conditions (3) are fulfilled immediately in the SGP due to the wide spatial spectrum of plasmons. These conditions can be rewritten as $k^2 c^2 = (3/2\omega_0)^2 - \omega_p^2$, which gives the ‘‘radiation circle’’ in the $k_x k_y$ plane. Figure 3(a) shows the spatial spectrum of electromagnetic waves in the simulation box filtered near the $3/2\omega_0$ frequency. One can see two waves with $k_x \approx \pm 0.7 \frac{\omega_0}{c}$ sitting exactly at the radiation circle and the third wave at $k_x \approx 2 \frac{\omega_0}{c}$ near the circle. Emission of the harmonic field A is governed by the equation $(\frac{1}{c^2} \frac{\partial^2}{\partial t^2} - \nabla^2 + \frac{\omega_p^2}{c^2})A = \frac{4\pi}{c} \mathbf{j}(3/2\omega_0)$. Hence, the spatial spectrum of the $\mathbf{j}(3/2\omega_0)$ source must also intersect the radiation circle to get efficient THH emission.

The velocity $\mathbf{v}_{\text{osc}}(x, y, t)$ has to be calculated to obtain a spatial spectrum of the linear source $\mathbf{j}_{\text{lin}}(3/2\omega_0)$. It was done using Newton’s law $m_e \frac{\partial \mathbf{v}_{\text{osc}}}{\partial t} = -e\mathbf{E}$, where the electromagnetic field \mathbf{E} was filtered near ω_0 . The source $\mathbf{j}_{\text{lin}}(3/2\omega_0) = \rho(\omega_0/2)\mathbf{v}_{\text{osc}}(\omega_0)$ was calculated using a band-pass filter at $3/2\omega_0$ frequency; an appropriate band-pass filter was used for both ρ and \mathbf{v}_{osc} before multiplication. The resultant spatial spectrum is shown in Fig. 3(b). There are two sources at $k_x \approx 2 \frac{\omega_0}{c}$ with high amplitudes and at $k_x \approx 0.64 \frac{\omega_0}{c}$ with a much lower amplitude. The width of the spatial spectrum along the y axis $\Delta k_y \sim \frac{\omega_0}{c}$ for the plasma with $L \sim \lambda$. Hence, the second source intersects the radiation circle providing a gener-

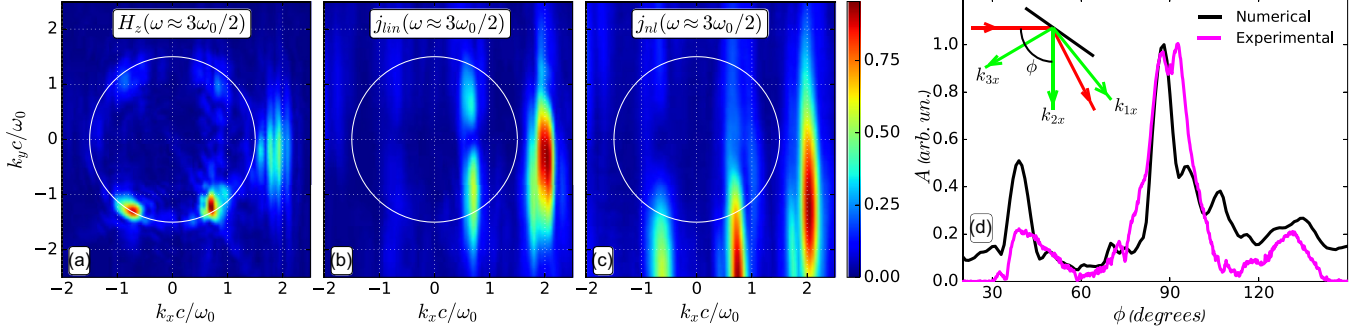


FIG. 3. Spatial spectra (normalized to their maxima) of H_z (a), current density j_{lin} (b), and current density j_{nl} (c) after $3/2\omega_0$ bandpass filtering. Wave vectors satisfying the condition (3) lie on a white circle. Angular spectra of THH emission obtained in the experiment (purple line) and from simulations (black line) (d). The inset shows incident and reflected laser beams (red arrows) and THH beams (green arrows).

ation of the THH immediately after excitation of the plasmon [$k_{2x} = k_{0x} + \kappa_{2x} \approx 0.64 \frac{\omega_0}{c}$ scattering process; Fig. 3(a)]. The first plasmon gives the $k_{1x} = k_{0x} + \kappa_{1x} \approx 2 \frac{\omega_0}{c}$ scattering, but this source cannot intersect the radiation circle, and the corresponding THH should not appear out of plasma. In any event, this current source is very strong and located not far from the radiation circle [Fig. 3(b)], while plasma is very steep. That is why the weak THH can be seen in Fig. 3(a) with $k_{1x} \approx 2 \frac{\omega_0}{c}$.

In Fig. 3(a) there exists an additional spatial component at $k_x \approx -0.7 \frac{\omega_0}{c}$ that is absent in the source $j_{\text{lin}}(3/2\omega_0)$. This THH arises as a consequence of nonlinearity of plasma waves at high (relativistic) laser intensities: the instability increment amounts to $\approx 0.05\omega_0$ already at $I \approx 10^{17} \text{ W/cm}^2$ near the quarter-critical density [5]. This is enough for plasma waves to become inharmonic over the duration of the laser pulse, i.e., high spatial harmonics $\propto \exp[-i(q\omega_p t - qk_{1(2)}x)]$, $q = 2, 3, \dots$ appear. The source of the THH $j_{\text{nl}}(3/2\omega_0) = \rho(2\omega_0/2)\mathbf{v}_{\text{osc}}(\omega_0/2)$ can be considered, where $\rho(2\omega_0/2)$ is the second harmonic of plasma waves and $\mathbf{v}_{\text{osc}}(\omega_0/2)$ is an electron quiver velocity in the plasmon or Stokes wave. Figure 3(c) shows the spatial spectrum of this source obtained applying the proper frequency bandpass filters to the ρ and \mathbf{v}_{osc} quantities. Thus, we obtain radiation sources with wave numbers $k_{1x}^{\text{nl}} = 2\kappa_{1x} + \kappa_{2x} = 2\kappa_{1x} + k_{sx} \approx 1.97 \frac{\omega_0}{c}$, $k_{2x}^{\text{nl}} = \kappa_{1x} + 2\kappa_{2x} \approx 0.64 \frac{\omega_0}{c}$, and $k_{3x}^{\text{nl}} = 2\kappa_{2x} + \kappa_{2x} = 2\kappa_{2x} + k_{sx} \approx -0.69 \frac{\omega_0}{c}$. Note that longitudinal electron oscillations generate a longitudinal current that cannot emit an electromagnetic wave in homogeneous plasma, but this is allowed in the steep-gradient plasma [23]. The first two sources coincide with sources from $j_{\text{lin}}(3/2\omega_0)$, but the third source is a new one and results from plasma waves nonlinearity. This nonlinear source generates the THH with $k_{3x}^{\text{nl}} = -0.69 \frac{\omega_0}{c}$ in Fig. 3(a). Thus, by measuring the THH spatial spectrum (which is quite easy to realize experimentally) one can gain insights into the behavior of strongly nonlinear plasma waves.

VI. EXPERIMENTAL VERIFICATION

Dedicated experiments were made to verify the picture of the THH generation described above. A Ti:sapphire laser system was used with maximum pulse energy at the target $W = 50 \text{ mJ}$, its shortest duration $\tau = 50 \text{ fs}$, and intensity I

up to $5 \times 10^{18} \text{ W/cm}^2$. The peak to amplified spontaneous emission (ASE) pedestal ratio was 10^8 (10 ps prior to the main pulse). The p -polarized laser radiation was obliquely focused onto the thick molybdenum target by an off-axis parabolic mirror (the focal length $F \sim 7.5 \text{ cm}$, $\alpha = 60^\circ$). An additional pulse from the Q-switched Nd:YAG laser (pulse duration 10 ns, maximal intensity at the target $\sim 10^{12} \text{ W/cm}^2$) created preplasma with the controlled scale length. Maxima of the Ti:sapphire and Nd:YAG pulses coincided both in space and in time. A color CCD camera equipped with interference filters (to reject 800 and 1064 nm radiation) measured plasma angular emission near the $3/2\omega_0$ frequency. A more detailed description of the setup, preplasma control, etc., can be found in Refs. [16,21]. In particular, the plasma scale length in the vicinity of n_c was estimated as $L \sim \lambda$ [21]. In this study, we used $\tau = 100 \text{ fs}$ and $I \gtrsim 10^{17} \text{ W/cm}^2$ to make a direct simulation-to-experiment comparison. This regime was chosen to obtain an angular distribution of the THH undisturbed by plasma turbulence, which is the case at higher intensities. Figure 3(d) compares experimental and numerical angular distributions of the THH. There are three main maxima at $\phi \approx 40^\circ, 90^\circ$, and 130° in both distributions. The second and third ones correspond to the linear THH source with $k_{1x,2x}$ wave vectors. Such a quantitative agreement supports our idea of immediate fulfillment of the phase-matching conditions in the SGP and the crucial role of the wide angular spectrum of the pump and plasma waves. Note that there are also impacts from the nonlinear source with $k_{1x,2x}^{\text{nl}}$ to those two maxima. The first maximum is generated exclusively due to the nonlinear THH source with the k_{3x}^{nl} wave vector, and this proves the feasibility of the THH generation due to plasma wave nonlinearity.

VII. GENERALIZATION TO HIGHER INTENSITIES

It is worth establishing ranges for the intensity I and scale length L in which the hybrid SRS-TPD instability dominates and the picture described above stays valid. The TPD threshold intensity is $\sim 5 \times 10^{16} \text{ W/cm}^2$ [15]. This can be considered as the lower limit. To find the upper limit, a number of simulations were performed with intensities 10^{17} to $2 \times 10^{20} \text{ W/cm}^2$ ($\tau = 100 \text{ fs}$) and different scale lengths $L = 0.25\text{--}8\lambda$. The amplitude of a plasma wave reaches the wave-breaking limit [28] in a few laser periods at intensities

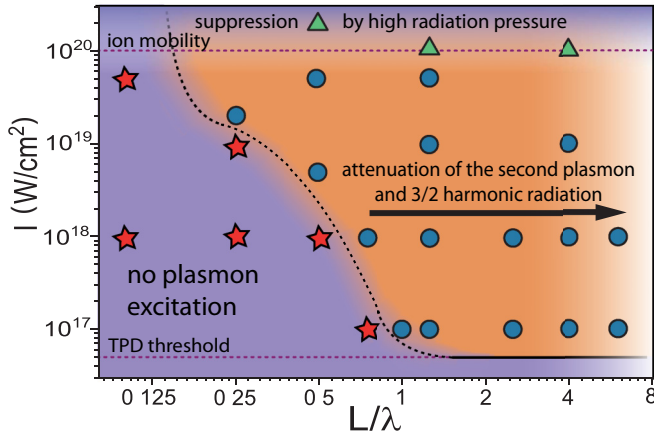


FIG. 4. Area of the SRS-TPD instability in the $L/\lambda - I$ plane ($\tau = 100$ fs). Blue circles show simulation points where the hybrid instability is essential, red stars show points where no instabilities arise, and green triangles show points where the radiation pressure becomes too high. The lower dashed line shows the TPD threshold from Ref. [15], while ion mobility should be taken into account above the upper dashed line [27].

$I \gtrsim 10^{18}$ W/cm², and the plasma becomes strongly turbulent. Nevertheless, preliminary Fourier filtration in the frequency domain allowed us to obtain spatial spectrum in which components of the hybrid instability are clearly visible [see Fig. 2(f), calculated 10 fs before the instant that the intensity reaches its maximum value of $I = 10^{19}$ W/cm² at the turning point]. Here plasma waves are excited by the leading front of the laser pulse up to the wave-breaking amplitude. The reflected intensity is low at this instant, and the spectrum in Fig. 2(f) contains significant components only in the first and third quadrants. The spatial spectrum of plasmons became broadened and complicated, but the mean κ_x values are almost the same. The small shift in κ_x values is due to the lower angle of incidence.

Figure 4 shows the area where the hybrid SRS-TPD instability prevails in the $L/\lambda - I$ plane. The hybrid instability may develop at the front of the laser pulse with an intensity $I > 5 \times 10^{19}$ W/cm², but further the plasma profile is steepened by the high intensity of laser radiation, and other processes govern plasma dynamics. The SRS process dominates if $L \gtrsim 5\lambda$, and the second plasma wave, corresponding to the TPD is getting weaker with an increase in L/λ . The hybrid instability first occurs at $L \gtrsim 0.5 - 1 \lambda$ and subrelativistic intensities $I \sim 10^{17} - 10^{18}$ W/cm²; however, it comes into play even at $L = 0.25\lambda$ in the intensity range $\sim 5 \times 10^{18}$ to 10^{19} W/cm². In the parameter range, where the hybrid SRS-TPD instability develops, the plasmon κ_x -projections do not change much, so the general interaction pattern will remain the same. It is first due to the laser energy deposition in a narrow ($\sim \lambda$) area near the turning surface. The electron density corresponding to this surface depends mostly on the angle of incidence, but this surface is located quite close to the quarter-critical density surface if the plasma gradient is sharp, $L \sim \lambda$. In its turn, this leads to efficient excitation of plasmons in the vicinity of the quarter-critical density for a wide range of angles of incidence.

Second, at relativistic intensities the laser pulse itself modifies the electron density profile due to the ponderomotive pressure and relativistic effects, creating a region with the quarter-critical density where the hybrid SRS-TPD develops.

It's worth noting that ions were immobile in all the simulations. The intensity limit at which this assumption fails can be evaluated comparing electron and ion response time [27]. In the case of a strongly ionized heavy target $\tau_e/\tau_i \approx a_0/35$ (a_0 being the amplitude of the normalized vector potential), therefore contribution of ions can be omitted up to $\sim 10^{20}$ W/cm² (see upper dashed line in Fig. 4). Note that high radiation pressure might prevail at such high intensities. A more detailed description of the underlying processes will be presented in a separate publication.

VIII. CONCLUSIONS

In conclusion, the hybrid SRS-TPD instability plays the dominant role for an ultraintense laser-plasma interaction at an oblique incidence of the p -polarized pulse if intensity I is within the $\sim 10^{17}$ to 5×10^{19} W/cm² range and plasma scale length L in the ~ 0.25 to 5λ range (Fig. 4). Our study was done with pulse duration $\tau = 100$ fs. Obviously, boundaries in Fig. 4 change if much shorter (~ 10 fs), or much longer (~ 1 ps), pulses are considered, but the overall picture of the SRS-TPD instability stays valid. This instability is essential at relativistic intensities since wave breaking of excited plasmons creates a huge number of very fast relativistic electrons undergoing further acceleration and forming well-collimated beams with ~ 1 nC/J charge [16,17]. It can also be relevant to inertial confinement fusion in the fast ignition scenarios, providing electron injection towards the fuel core [29].

The typical spatial spectrum of plasmons in the steep-gradient plasma is close to the case of homogeneous plasma in the x -projection with $\kappa_x \sim 1.2 \frac{\omega_0}{c}$ and $-0.2 \frac{\omega_0}{c}$ but is very wide in the y -projection, $\Delta \kappa_y \sim \frac{\omega_0}{c}$. The 3/2 harmonic is efficiently generated in the vicinity of the quarter-critical surface due to immediate fulfillment of the phase-matching conditions between plasmons and the pump wave in a steep-gradient plasma, and this is another feature of the hybrid instability in such a plasma. Hence the 3/2 harmonic is a clear sign that experimental conditions fall into the above-mentioned ranges, and steep-gradient preplasma is being formed. The angular spectrum of the 3/2 harmonic contains rich and valuable information on the excited plasmons. In particular, second and higher harmonics of the nonlinear plasma wave may contribute to the angular spectrum of this plasma emission.

ACKNOWLEDGMENTS

The authors wish to thank V. Bychenkov, A. Brantov, and S. Bochkarev for numerous valuable discussions and advice with the Mandor PIC code. This work was done with financial support from the RFBR (Grants No. 19-32-60069 and 19-02-00104). Development of numerical methods used in Sec. V. was supported by RSF Grant No. 20-79-00051. Simulations were made using Moscow State University Supercomputing Facility “Lomonosov.” D.G. acknowledges the foundation for theoretical research “Basis” for financial support.

- [1] B. B. Afeyan and E. A. Williams, *Phys. Rev. Lett.* **75**, 4218 (1995).
- [2] R. K. Follett, J. G. Shaw, J. F. Myatt, J. P. Palastro, R. W. Short, and D. H. Froula, *Phys. Rev. Lett.* **120**, 135005 (2018).
- [3] D. Turnbull, A. V. Maximov, D. H. Edgell, W. Seka, R. K. Follett, J. P. Palastro, D. Cao, V. N. Goncharov, C. Stoeckl, and D. H. Froula, *Phys. Rev. Lett.* **124**, 185001 (2020).
- [4] B. B. Afeyan and E. A. Williams, *Phys. Plasmas* **4**, 3803 (1997).
- [5] W. L. Kruer, *The Physics of Laser Plasma Interactions* (Addison-Wesley, Redwood, CA, 1988).
- [6] A. G. Mordovanakis *et al.*, *Phys. Rev. Lett.* **103**, 235001 (2009).
- [7] V. M. Malkin, G. Shvets, and N. J. Fisch, *Phys. Rev. Lett.* **84**, 1208 (2000).
- [8] D. Turnbull, S. Bucht, A. Davies, D. Haberberger, T. Kessler, J. L. Shaw, and D. H. Froula, *Phys. Rev. Lett.* **120**, 024801 (2018).
- [9] D. Gordon *et al.*, *Phys. Rev. Lett.* **80**, 2133 (1998).
- [10] B. Quesnel, P. Mora, J. C. Adam, A. Héron, and G. Laval, *Phys. Plasmas* **4**, 3358 (1997).
- [11] S. Guerin, G. Laval, P. Mora, J. C. Adam, A. Héron, and A. Bendib, *Phys. Plasmas* **2**, 2807 (1995).
- [12] D. F. Gordon, B. Hafizi, R. F. Hubbard, and P. Sprangle, *Phys. Plasmas* **9**, 1157 (2002).
- [13] D. F. Gordon, B. Hafizi, P. Sprangle, R. F. Hubbard, J. R. Peñano, and W. B. Mori, *Phys. Rev. E* **64**, 046404 (2001).
- [14] L. Veisz, W. Theobald, T. Feurer, H. Schwoerer, I. Uschmann, O. Renner, and R. Sauerbrey, *Phys. Plasmas* **11**, 3311 (2004).
- [15] L. Veisz, W. Theobald, T. Feurer, H. Schillinger, P. Gibbon, R. Sauerbrey, and M. S. Jovanović, *Phys. Plasmas* **9**, 3197 (2002).
- [16] I. Tsymbalov *et al.*, *Plasma Phys. Controlled Fusion* **61**, 075016 (2019).
- [17] Y. Ma *et al.*, *Proc. Natl Acad. Sci. U. S. A.* **115**, 6980 (2018).
- [18] A. Tarasevitch, C. Dietrich, C. Blome, K. Sokolowski-Tinten, and D. von der Linde, *Phys. Rev. E* **68**, 026410 (2003).
- [19] M. C. Downer, R. Zgadaj, A. Debus, U. Schramm, and M. C. Kaluza, *Rev. Mod. Phys.* **90**, 035002 (2018).
- [20] I. N. Tsymbalov, D. A. Gorlova, V. Y. Bychenkov, and A. B. Savelev, *Quantum Electron.* **49**, 386 (2019).
- [21] K. A. Ivanov *et al.*, *Phys. Plasmas* **24**, 063109 (2017).
- [22] D. V. Romanov, V. Y. Bychenkov, W. Rozmus, C. E. Capjack, and R. Fedosejevs, *Phys. Rev. Lett.* **93**, 215004 (2004).
- [23] V. Ginzburg, *The Propagation of Electromagnetic Waves in Plasmas* (Pergamon, Oxford, 1970).
- [24] P. Mulser and D. Bauer, *High Power Laser-Matter Interaction* (Springer, Berlin, 2010).
- [25] R. W. Short, W. Seka, K. Tanaka, and E. A. Williams, *Phys. Rev. Lett.* **52**, 1496 (1984).
- [26] N. G. Basov, Y. A. Zakharenkov, A. A. Rupasov, G. V. Sklizkov, and A. S. Shikanov, *Dense Plasma Diagnostics* (Nauka, Moscow, 1989).
- [27] K. Jiang, C. T. Zhou, T. W. Huang, C. N. Wu, L. B. Ju, H. Zhang, S. Z. Wu, T. X. Cai, B. Qiao, M. Y. Yu, and S. C. Ruan, *Phys. Rev. E* **98**, 033206 (2018).
- [28] J. Wang, G. L. Payne, and D. R. Nicholson, *Phys. Fluids B* **4**, 1432 (1992).
- [29] J. Badziak, S. Jabłoński, and J. Wołowski, *Plasma Phys. Controlled Fusion* **49**, B651 (2007).